Coupling *in situ* atomic force microscopy (AFM) and ultra-small-angle X-ray scattering (USAXS) to study the evolution of zinc morphology during electrodeposition within an imidazolium based ionic liquid electrolyte

Jayme S. Keist [a, b, 1], Joshua A. Hammons [b], Paul K. Wright [c], James W. Evans [a], Christine A. Orme [b, *]

[a] *210 Hearst Mining Building, University of California, Berkeley, CA, 94720, USA*
[b] *Lawrence Livermore National Laboratory, 7000 East Ave. Livermore, CA, 94550, USA*
[c] *330C Sutardja Dai Hall, University of California, Berkeley, CA, 94720, USA*

ARTICLE INFO

ABSTRACT

Zinc (Zn) is a low-cost material that is widely used in plating and is under consideration as a reversible deposit for a range of energy storage applications. In recent years, researchers have demonstrated that the Zn morphology can be tuned by electrodepositing from an ionic liquid often leading to morphologies that improve cyclability. However, the underlying mechanisms that control deposition and morphology are not well understood. In this work, we evaluate the evolution of zinc morphology as a function of the deposition thickness using *in situ* atomic force microscopy (AFM), *in situ* ultra-small angle X-ray scattering (USAXS) and *ex situ* electron microscopy. Imaging reveals two dominant features: a hexagonal plate-like morphology associated with individual Zn crystals and larger domains in which the individual crystals appear co-aligned. Analysis of the key features observed by USAXS indicates that the growth of the domain size is non-linear with the charge passed and that at least some of this non-linearity can be attributed to increased coalescence of the individual plates as the deposit thickens. A more detailed analysis suggests that there is little change in the aspect ratio of the individual Zn crystals — this is consistent with a growth mechanism in which previously deposited plates grow in diameter as new plates nucleate on their surface and then coalesce into one crystal.

1. Introduction

There is considerable interest in using zinc (Zn) for energy storage applications [1–4] including Zn-air [3–6] and flow batteries [7,8] but commercial use has been limited due to the relatively poor cyclability [2]. This poor cyclability is typically the result of the propensity of the zinc electrode to form detrimental morphologies during growth, such as dendrites, nodules, and filaments [9,10]. Non-aqueous electrolytes, including ionic liquid systems, have shown good applicability in electrodeposition of metals with advantages that includes a wider potential window and higher thermal stability [11–13]. The use of ionic liquid based electrolytes instead of conventional aqueous based electrolytes has shown promise in reducing the formation of detrimental morphologies and forming a more uniform metal film during electrodeposition [14,15].

For zinc electrodeposition within ionic liquid based electrolytes, most studies have used the pyrrolidinium or imidazolium family of cations with anions that include chloride (Cl), dicyanamide (DCA), trifluoromethylsulfonate (TfO), and bis(trifluoromethanesulfonyl) imide $(Tf_2 N)_2$; the zinc precursor within the electrolyte has included $ZnCl_2$, zinc triflate $(Zn(TfO)_2)$, and $Zn(Tf_2 N)_2$ [16–23]. Electrodeposition of zinc within the imidazolium family generally produces crystalline films exhibiting well-defined hexagonal facets [16,17,19,24,25]. In a recent investigation, Liu et al. [25] investigated

---

* Corresponding author.
    E-mail addresses: keist@psu.edu (J.S. Keist), hammons3@llnl.gov (J.A. Hammons), pwright@me.berkeley.edu (P.K. Wright), evans@berkeley.edu (J.W. Evans), orme1@llnl.gov (C.A. Orme).
  [1] Present Address: The Pennsylvania State University, P.O. Box 30, State College, PA 16804 USA.

the electrodeposition morphology of zinc within 1-ethyl-3-methylimidazolium (EMIm) trifluoromethylsulfonate (TfO) electrolyte with 0.1 mol dm^{-3} Zn(TfO)$_2$ and 0.015 mol dm^{-3} Ni(TfO)$_2$ and found that the zinc deposition morphology was compact and exhibited co-aligned hexagonal platelets. In the presence of water, in the imidazolium family of ionic liquids, the zinc deposition morphology may exhibit non-textured, rounded zinc deposits [26,27]. Electrodeposition of zinc within the pyrrolidinium family generally tends to exhibit smaller crystallites with more rounded morphologies [19,20,22,23,27−29]. The evolution of the textured zinc morphology is the focus of this study and builds upon our recent work [30] where highly textured, zinc platelets were organized into domains of co-aligned platelets. This morphology was deposited from 1-butyl-3-methyl-imidazolium (BMIm) cation and trifluoromethanesulfonate (TfO) anion which is the same system used in this study.

In the BMIm TfO electrolyte, zinc crystalize in the form of hexagonal plates reflecting their underlying hexagonal symmetry. The thin plate morphology is evidence of an anisotropic growth rate with the basal facets growing 5−10 times slower than the prism facets. Collectively, as observed by *in situ* atomic force microscopy (AFM) [30], the Zn domains form a compact, polycrystalline surface film, and the surface morphology roughened slowly with increasing film thickness whereby under some conditions, the roughness plateaued and stopped increasing with continued growth [30]. During the initial deposition, the zinc plates appeared to nucleate in random orientations, but two phenomena altered the film texture as growth proceeded. First, crystals that nucleated with their basal facet parallel or nearly parallel to the substrate (basal-oriented) were overgrown by crystals that nucleated with their prism facet parallel to the substrate (prism-oriented) because the prism facets grew faster. For this reason, over time, the deposited zinc surface became dominated by prism-oriented plates. And second, new islands preferentially nucleated on the basal facet leading to stacked plates that ultimately formed domains where the basal facets of the plates were aligned. We postulate that this desirable cessation of roughening results from this pattern of growth − the surface evolves to a state exhibiting prism-oriented surface resulting in a similar growth rate across the surface − that leads to uniform growth. Therefore, the coalignment and evolution in domain orientation can change the bulk film roughness for a specified film thickness.

From the *in situ* AFM study of the direct spatial analysis of the zinc surface during deposition within an BMIm TfO electrolyte, several parameters emerge: the diameter and thickness of the individual plates, the size of the domains, and the degree of prism texture [30]. There are drawbacks, however, to this technique. These drawbacks include the relatively small scanning area (typically on the order of microns), the potential for tip-surface interactions, apparent broadening of lateral features due to tip size, and the limited ability of the AFM tip to follow a surface with deep crevices or complicated morphologies with large height to width aspect ratios. To help counteract these drawbacks and to provide a complementary view, we examined the growth parameters that emerged from the AFM analysis using X-ray scattering techniques, that have the advantage of sample averaging through the volume of the film, but often suffer from model ambiguity in cases where only a smooth intensity curve is obtained.

In this study, ultra-small angle X-ray scattering (USAXS) was employed to help elucidate the growth characteristics of zinc during electrodeposition within an BMIm TfO electrolyte. USAXS is a volume-average technique that can obtain nano-scale to micron scale information through the entire irradiated sample volume [31,32]. In the USAXS regime, the scattering of X-rays results from spatial fluctuations of the electron density within the material and is used in this study to extract changes in the zinc morphology while the film is growing during deposition. Determining the real space structure from USAXS requires fitting the scattering data to a model. It is often the case for complex systems that the small angle scattering is ambiguous and could be attributed to multiple phases (i.e. particles and pores). While a heuristic X-ray scattering model can be used to extract non-specific information from the data, such as relevant length scales, complementary imaging techniques can help develop a specific model that can extract physically meaningful information about the phase from the X-ray scattering. To help develop a specific small angle scattering model for the zinc electrodeposition within the BMIm TfO electrolyte, this study used *in situ* AFM imaging and *ex situ* electron microscopy to develop a specific small angle scattering model for the deposits and this model was then compared with a non-specific heuristic model that uses known small angle scattering approximations [33].

2. Experimental

2.1. Electrochemical measurements and electrodeposition procedure

The ionic liquid electrolyte was prepared by dissolving zinc trifluoromethanesulfonate (Zn(TfO)$_2$, Sigma-Aldrich, 98%) at a temperature of 80 °C within 1-butyl-3-methyl-imidazolium trifluoromethanesulfonate (BMIm TfO, IoLiTec Ionic Liquids Technologies, >99%). Removal of residual water and impurities was conducted following the recommendations of Gnahm and Kolb [34]. This procedure included adding 3 Å molecular sieves (Fluka) to the electrolyte and drying the electrolyte at 100 °C under a low vacuum of 3.3 × 10^3 Pa for a minimum of 24 h. After drying, the resulting electrolyte was clear with a slight amber color. To help maintain low water content during the experiments, molecular sieves (Fluka) with 3 Å pores were added to the ionic liquid electrolyte for the electrochemical measurements as well as for the USAXS and AFM Zn deposition experiments. In addition, for the electrochemical measurements and AFM experiments, argon gas was percolated into the electrolyte through a port on the cell to further control the moisture within the electrolyte.

Electrochemical measurements along with the AFM and USAXS Zn deposition experiments were conducted with the aid of a Bio-Logic SP-300 potentiostat/galvanostat and EC-Lab® software (version 10.23). The working electrode for all experiments was a platinum disk substrate where the substrate was sputter deposited to a thickness of 0.6 μm on a 0.5 mm thick glass wafer. The root mean square (RMS) surface roughness of the sputter deposited Pt surface measured by AFM was 3.5 ± 0.5 nm. A 1 mm diameter electrode (7.85 × 10^{-3} cm^2 area) was used for the electrochemical measurement and AFM Zn deposition experiments, and a 2 mm diameter electrode (3.14 × 10^{-2} cm^2 area) was used for the USAXS Zn deposition experiment. To remove contaminants the Pt substrate was cleaned by submerging within 1 M H$_2$SO$_4$ for 5 min and subsequently washed with Millipore water. Residual organics were removed by plasma etching within a Harrick Plasma cleaner (Model PDC-32G) for 3 min. The electrochemical measurements and AFM Zn deposition experiments were conducted within a PEEK electrochemical AFM cell (Asylum Research). For the USAXS experiment, electrodeposition of zinc was conducted within an enclosed polyether ether ketone (PEEK) cell using a design by El-Dasher and Torres [35]. For all experiments, Zn wire (Alfa Aesar, 99.995%) was used for both the counter and reference electrodes.

For the Zn electrodeposition experiments, the Pt substrate was initialized by the potentiostatic reduction of zinc on the surface (−500 mV for the AFM experiments and −600 mV for the USAXS experiment versus the Zn reference wire) for a total charge passed

of 52.3 mC cm^{-2}. The zinc deposit was removed by potentiostatic oxidation at +200 mV versus the Zn reference wire. This initiation step improved the uniformity of subsequent depositions on the Pt substrate as observed visually from the optical microscope.

As commonly done with ionic liquid systems [17], the electrodeposition overpotential, η, was defined as the difference between the applied potential, E_{app}, and the observed crossover potential, E_{CO}. An example of the observed crossover potential, E_{CO}, for this system as found by cyclic voltammetry is shown in Ref. [30] and in the Results section of this article. To account for the uncompensated resistance, R_u, the electrodeposition overpotential was estimated by $\eta = |E_{app} - iR_u - E_{CO}|$, where i was the average current measured during zinc deposition. The uncompensated resistance of ionic liquid electrolyte systems can be significant since ionic liquid systems exhibit relatively low ionic conductivities compared to supported aqueous electrolyte systems [15]. In addition, the limitations of the cell geometry for both the AFM and USAXS electrochemical cells did not allow placement of the reference zinc wire near the deposition surface. For the AFM cell, the reference wire was placed 10 ± 1 mm from the deposition surface and R_u was measured at $1700 \pm 200\,\Omega$ by the current interrupt method [36]. For the USAXS electrochemical cell, the reference wire was located 15 ± 1 mm from the deposition surface and R_u was estimated at $2600 \pm 500\,\Omega$.

In this investigation, the charge density passed during electrodeposition of zinc is reported in terms of both mC cm^{-2} and Zn monolayers (ML). The use of Zn ML allows for inferring the resulting Zn film thickness from the amount of charge passed during electrodeposition. The charge density relationship between Zn ML and mC cm^{-2} was calculated assuming 100% current deposition efficiency and randomly oriented grains with an average atomic spacing of Zn at 0.248 nm. Following these assumptions, 100 Zn ML corresponds to 52.3 mC cm^{-2}. From the previous study [30], the assumptions appeared to be valid since the film thickness measurements made by AFM were within 90% of the calculated Zn ML values.

2.2. Ultra-small angle X-Ray scattering (USAXS) experiment

In situ USAXS measurements were performed at the Advanced Photon Source (APS) located at Argonne National Laboratory, Illinois, USA on sector 15-ID-B (now 9-ID-B) using monochromatic 17 keV X-rays ($\lambda = 0.72$Å). The USAXS instrument was combined with a two-dimensional wide-angle X-ray scattering (WAXS) detector and a pinhole small-angle X-ray scattering (SAXS) camera. The Bonse-Hart USAXS instrument measures the scattered intensity from a sample area of 1.2 mm^2 as a function of angle, θ, where $\theta = 0°$ is perpendicular to the substrate surface and $\theta = 90°$ is parallel. In calculations and drawings, the photon flux is in the x-direction and the sample is parallel to the y-z plane. The angular range of the instrument allowed measurement within a q-range from 10^{-4} Å^{-1} to 6 Å^{-1}. The scattered intensity collected from this instrument provided information about mesoscale dimensions that are oriented out of plane with the X-rays. This means that heterogeneities oriented in the angular range between perpendicular and parallel to the surface could be resolved. However, the scattered intensity collected from this geometry was slit-smeared with dimensions only parallel to the surface [37,38]. In cases where the scattering heterogeneities are statistically isotropic, this smearing effect was accounted for within the Irena software by knowing the slit-length, q_{slit}, that was calculated directly from the instrument geometry [37,38]. In the case where some preferential orientation of the Zn deposit (i.e. anisotropic scattering), the slit-smearing becomes more complicated since the scattering in the two directions is different. Because it is unclear whether the Zn deposit is statistically isotropic or has some preferred orientation, both possibilities are presented in this study. Nevertheless, all USAXS/SAXS/WAXS data were plotted as the intensity versus the magnitude of the vertical scattering vector, **q**, where its modulus, q, is defined as:

$$q = 4\pi \frac{\sin \theta/2}{\lambda} \qquad (1)$$

Detailed information and capabilities of the instrument are found elsewhere [37,38].

To minimize electrolyte damage during scanning from the high energy X-ray beam, Al and Ti filters were inserted into the incident beam that effectively reduced the number of photons per unit time. In addition, the beam was blocked during electrodeposition to assure that beam interactions would not interfere with the zinc deposition.

Zinc electrodeposition was conducted potentiostatically with a series of potential steps with an applied potential, E_{app}, of -700 mV versus the Zn reference wire. During electrodeposition, the resulting iR_u drop was estimated at 110 ± 30 mV and E_{CO} averaged -220 ± 10 mV versus the zinc reference, resulting with an estimated electrodeposition overpotential, η, of 370 ± 40 mV and was within the range of the zinc deposition trials for the AFM experiments (from 245 to 445 mV) [30]. Between the applied potential steps, the substrate was held at a slightly reducing potential of -10 mV versus E_{CO} to avoid dissolution of the Zn and allow for the USAXS scan (≈ 9 min).

Chronoamperograms for the Zn electrodeposition within the USAXS cell are shown in Fig. 1. The first three potential steps at the applied potential was conducted until 400 Zn ML (209.2 mC cm^{-2}) of charge passed and USAXS scans were obtained after 400 Zn ML and 1200 Zn ML of total charge passed. Subsequent USAXS scans were obtained after applied potential steps of 800 Zn ML (418.4 mC cm^{-2}) until a total of 3600 Zn ML (1882.8 mC cm^{-2}) of charge was passed. For the first potentiostatic step to 400 Zn ML, the current initially exhibited a peak and then steadily decreased approaching steady state suggesting nucleation and diffusion limited growth. Subsequent potential steps showed a rapid decrease in current density to a steady state value of around 0.85 mA cm^{-2} suggesting diffusion limited growth. Peaks were not observed in the subsequent potential steps and was assumed to be the result of the sluggish kinetics of the system. After the final USAXS scan of the Zn deposition after 3600 Zn ML of charge passed, the Al and Ti filters were removed and a WAXS image was obtained.
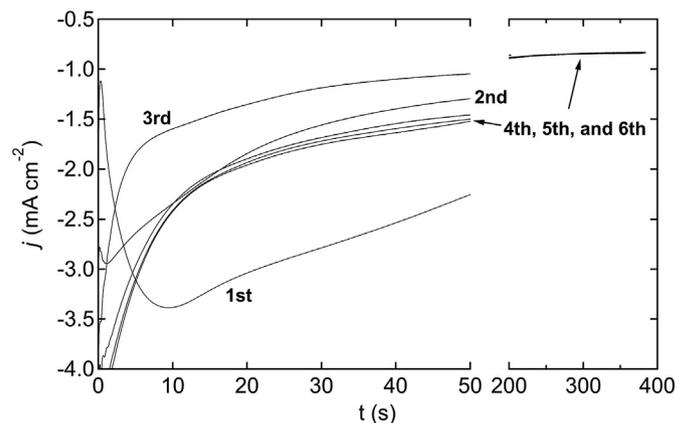
Fig. 1. Chronoamperograms of zinc deposition in 0.34 mol kg^{-1} Zn(TfO)$_2$/BMIm TfO within the USAXS electrochemical cell at an estimated overpotential of 370 mV. The total charge passed for the 1st, 2nd, and 3rd potential steps was 400 Zn ML (209.2 mC cm^{-2}) and for the 4th, 5th, and 6th potential steps was 800 Zn ML (418.4 mC cm^{-2}).

For USAXS data reduction, the USAXS scan used for background subtraction was obtained from a separate Pt substrate immersed within the ionic liquid electrolyte. This separate scan was required since it appeared that illuminating the Pt substrate with the X-ray beam prior to zinc deposition resulted in a possible breakdown of the ionic liquid electrolyte on the substrate surface that interfered with the subsequent nucleation and growth of zinc.

Data reduction was conducted with the Indra2 package [37] within Igor Pro (version 6.37), whereby the USAXS from the Pt substrate and ionic liquid were subtracted from the USAXS data obtained after deposition. Since the true zinc layer thickness during the USAXS scans was unknown, data reduction was conducted assuming a constant zinc deposition thickness (1 mm); for this reason, the intensity scaling is arbitrary but comparable between scans. This assumption would not impact the morphological analysis conducted in this investigation since the thickness only affects the scaling of the scattering intensity, $I(q)$, and not the shape.

2.3. Atomic force microscopy (AFM) experiments

AFM imaging of the zinc electrodeposition was performed in contact mode on an Asylum MFP3D instrument using a silicon nitride tip on a silicon nitride cantilever (Olympus TR800PSA). The zinc surface was imaged with a 4 μm × 4 μm area with 512 lines and 512 points per line corresponding to ~8 nm pixel resolution. The vertical resolution of the AFM instrument was ~0.1 nm. Further details of the electrochemical AFM cell and the AFM setup are found in Ref. [30]. AFM image analysis and measurements were conducted within Gwyddion (version 2.52) [39].

For the AFM experiments, several series of zinc deposition trials were conducted potentiostatically with current pulses where, for each pulse, 200 Zn ML (104.6 mC cm^{-2}) of charge was passed. AFM imaging was conducted at periodic intervals throughout the film growth between current pulses. To assure that the Zn surface did not undergo dissolution that would occur at open circuit potential (OCP), AFM imaging of the Zn surface was conducted while the substrate was held at a slightly reducing potential of 10 mV below E_{CO}. The holding time required for AFM imaging was approximately 10 min. Growth and imaging proceeded until a total of 2800 Zn ML (1464.4 mC cm^{-2}) of charge was passed. For each series of depositions, zinc was deposited at different applied potentials, E_{app}, of −400, −500, −650 mV versus a Zn reference wire. For these deposition trials, the deposition overpotential, η, was estimated at 245, 325, and 445 mV vs. E_{CO}, respectively [30]. As with potentiostatic deposition within the USAXS cell, the current profile during deposition within the AFM cell remained consistent in magnitude and shape suggesting that the electrochemical environment was not changing significantly during growth [30].

2.4. Electron microscopy of the zinc surface

For ex situ electron microscopy of the zinc deposition morphology after deposition within the USAXS electrochemical cell, a separate deposition trial was conducted outside of the USAXS instrument. This separate trial was required since the added time needed to extract the electrochemical cell out of the USAXS instrument allowed for significant dissolution of the zinc surface as it remained at OCP for several minutes prior to extracting and washing. The deposition of zinc within the USAXS electrochemical cell mirrored the same electrochemical parameters as was conducted within the USAXS instrument including holding times.

For ex situ SEM analysis of the zinc deposited surface after both the USAXS and AFM experiments, the substrate was washed with ethanol and Millipore water (18 ohm-cm) and dried. Electron microscopy was conducted on a JEOL JSM-7401F FESEM scanning electron microscope (SEM).

2.5. Zinc domain size measurements from imaging

The average zinc domain sizes were estimated by direct measurements conducted on both the AFM and the SEM images by manually outlining the observed domains and measuring the average domain area within ImageJ (ver. 1.51). Domains located on the edges of the images were not included in the measurements. Measuring the zinc domain sizes was equated to measuring grain sizes as outlined by ASTM E112, Standard Test Methods for Determining Average Grain Size [40], where the mean zinc domain diameter and its standard deviation are given by the mean and standard deviation of the square root of the measured domain areas.

3. Results and discussion

We first describe the electrochemical behavior of the BMIm TfO based electrolyte where the results suggest slow kinetics and diffusion-limited growth. Next, we describe the results from in situ X-ray scattering, demonstrating that two length scales emerged. By showing that deposition of zinc within the AFM and USAXS cells resulted in similar zinc morphology, we could then use imaging to interpret the scattering from the USAXS analysis. Imaging showed that zinc deposition consisted of stacked hexagonal plates that led to two length scales: the plate thickness, t_p, and the plate radius, R_p. In situ AFM data was also used to show how the nucleation behavior led to domain formation and the evolution of film texture. The domain geometry was approximated as cylinders composed of stacked plates with nominal radius, R_p, and domain thickness, $t_d = N \times t_p$, where N is the number of plates within a domain. The USAXS data was first described in terms of a generalized model (unified model) with scattering from the thickness and diameter of the plates. In the supplementary information we describe a more complex, oriented cylinder model that attempted to capture the organization of plates into domains and the rotation of the plate orientation from random to textured in keeping with AFM observations. Although the oriented cylinder model was consistent with the X-ray scatter data, it did not add definitive information beyond what was found with the simpler unified model.

3.1. Electrochemical measurements

Cyclic voltammetry and chronoamperometry were used as a foundation to investigate the BMIm TfO system. Fig. 2 shows the cyclic voltammograms (CV) of a Pt electrode in 0.34 mol kg^{-1} Zn(TfO)$_2$/BMIm TfO with various scan rates at 25 °C. Cathodic peaks were observed from −0.63 to −0.77 vs. the Zn wire where cathodic peaks shifted to more negative values with higher scan rates. Anodic peaks were observed around +0.22 to +0.24 vs the Zn wire. As shown Fig. 2a, the BMIm TfO without Zn(TfO)$_2$ did not show cathodic or anodic peaks and exhibited a stability window of around 2.6 V. The cathodic peak was attributed to the reduction of Zn(II) to Zn and the anodic peak was attributed to dissolution of the Zn deposited on Pt electrode from the prior cathodic scan. The Zn(II)/Zn reaction on the Pt electrode was considered electrochemically irreversible because there was a large peak separation and the cathodic peaks shifted to more negative values with increasing scan rates. The wide spacing in the CV is indicative of an irreversible redox reaction with a relatively high activation energy and slow kinetics. In addition, the integrated current during the anodic scan was 90 ± 0.5% of the cathodic scan suggesting that either there was a parasitic cathodic reaction or that not all the Zn deposited during the cathodic scan underwent dissolution. Finally,
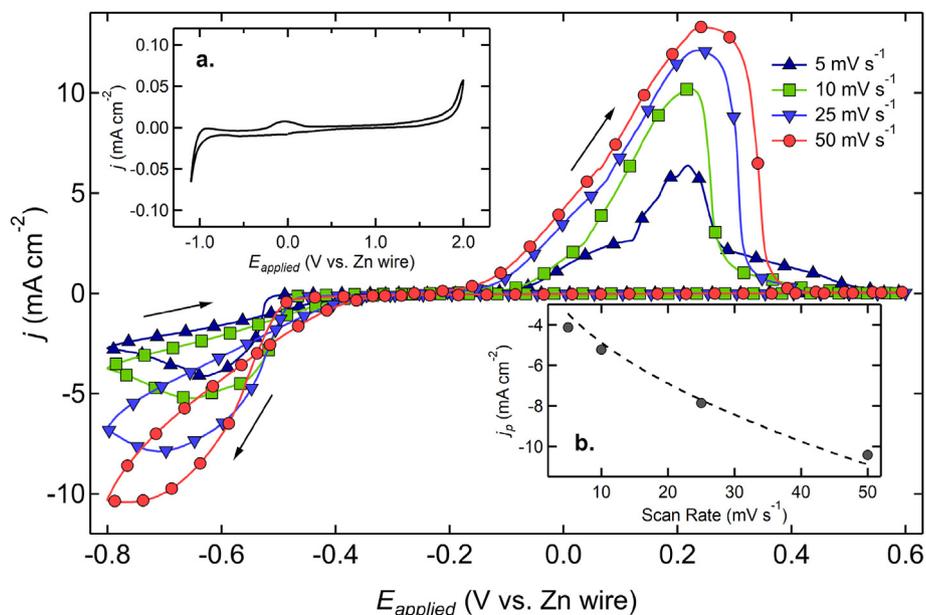
Fig. 2. Cyclic voltammograms (CV) of a Pt electrode in 0.34 mol kg^{-1} Zn(TfO)$_2$/BMIm TfO at 25 °C at scan rates of 5, 10, 25, and 50 mV s^{-1}. Arrows show the direction of the scan. Inset (a) shows a CV of the Pt electrode within neat BMIm TfO at a scan rage of 10 mV s^{-1} at room temperature. Inset (b) shows the peak cathodic current density, j_p, plotted against the scan rate where the dashed line corresponds to the best fit curve following $j_p^{0.5}$.

the peak cathodic current density approximately followed a square root relationship with the CV scan rate (Fig. 2b). This relationship is consistent with diffusion-limited growth where electron transfer is direct with electrode rather than via a multi-step reaction such as adsorption of electrolyte followed by electron transfer [36].

Chronoamperometry data was collected for various potential steps to evaluate the electrochemical behavior of Zn(II) within the BMIm TfO system. Fig. 3 shows the chronoamperograms of the Pt substrate in in 0.34 mol kg^{-1} Zn(TfO)$_2$/BMIm TfO at 25 °C. For the various potential steps, current peaks were observed suggesting nucleation of Zn followed by converging of the current density with time following the expected behavior of a diffusion limited system.

The diffusion coefficient was estimated assuming the system most closely matches a disk electrode in a semi-infinite system where the reduction process is diffusion limited [36,41]. Using the analytical solution obtained by Aoki et al. [41], the diffusion coefficient of Zn(II) at 25 °C was estimated at 1.5 × 10^{-7} cm^2 s^{-1}. The estimated diffusion coefficient is within the range reported at room temperature for imidazolium based ionic liquids (from 1 to 12 × 10^{-7} cm^2 s^{-1} [42]) where these relatively low values are due to the high viscosity of the ionic liquid systems [42].

The nucleation behavior was inferred from the chronoamperometry data by plotting the data non-dimensionally with j^2/j_m^2 versus t/t_m where j_m is the peak current density and t_m is the
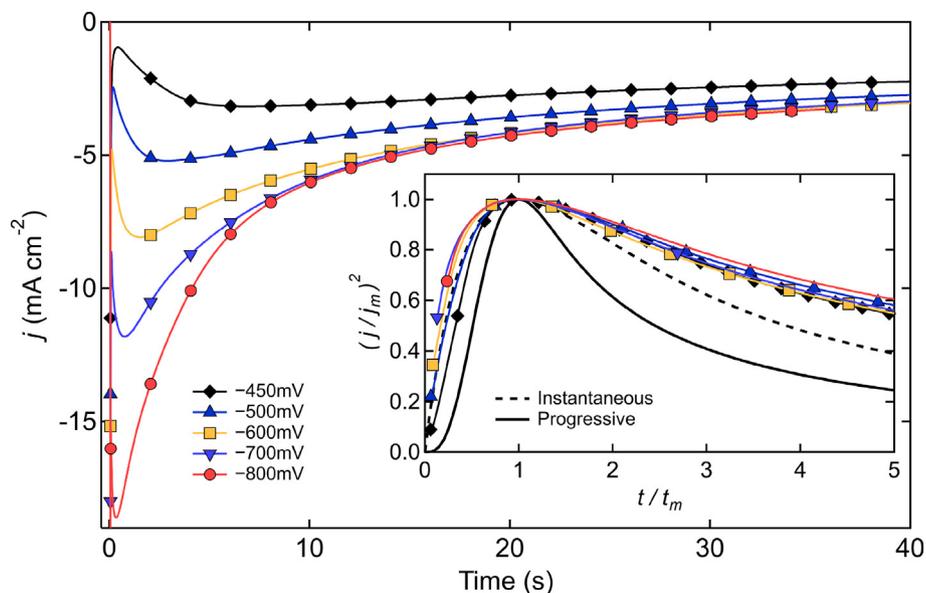
Fig. 3. Chronoamperograms of a Pt electrode in 0.34 mol kg^{-1} Zn(TfO)$_2$/BMIm TfO at 25 °C for various applied potentials vs. Zn wire. The inset figure shows the data normalized to the maximum current density and the corresponding time where the solid and dashed lines correspond to the theoretical models for progressive and instantaneous nucleation.

corresponding time, t. The resulting current transient peaks was compared to the Scharifker-Hills nucleation and growth models for both progressive and instantaneous nucleation [43] shown in the inset figure in Fig. 3. For all the scans, the data most closely followed the instantaneous nucleation model, and from this result, it was assumed that the initial stage of Zn deposition on the Pt electrode exhibited instantaneous nucleation under diffusion control.

3.2. Ultra small angle X-ray scattering (USAXS) measurements

Five USAXS scans were obtained during the electrodeposition of zinc on a Pt substrate within the 0.34 mol kg^{-1} Zn(TfO)$_2$/BMIm TfO electrolyte up to a final deposition of 3600 Zn ML (1882.8 mC cm^{-2}) of charge passed. The calculated slit smeared intensity after data reduction (background subtraction) for the five USAXS scans is shown in Fig. 4. In the high-q range ($q > 0.05$ Å^{-1}), there was a high level of background noise that impeded analysis of the structural data. The mid-q range ($0.002 < q < 0.05$ Å^{-1}) was identified as the power-law region and contains information about the surface roughness [44] and/or the anisotropy of the domains. This region is therefore ambiguous and model dependent; the unified model assumes that the surface is fractal-like in nature where the surface contains some roughness, while the oriented cylinder model assumes some anisotropy (see Section 3.4.2 and Supplementary). In this region, the intensity from each scan appeared to decay at roughly the same power-law slope (between -3.44 to -3.74) suggesting that the interface structure between the zinc surface and the ionic liquid electrolyte remained mostly unchanged during the electrodeposition. Finally, within the low-q range ($q < 0.002$ Å^{-1}), Guinier regions [45] were observed where the intensity exhibited a knee as the scattering intensity behavior transfers from power-law scaling regime. The location of the Guinier regions occurred at lower q values with increasing amounts of charge passed suggesting that the average size of the Guinier scattering entities increased with increasing deposition thickness. In addition, after electrodeposition of 2000 Zn ML, a second Guinier

was observable in the higher q range of around 0.02 Å^{-1} as shown in Fig. 4a.

After electrodeposition of the Zn within the USAXS cell to a total of 3600 Zn ML (1882.8 mC cm^{-2}) of charge passed, a WAXS image was obtained of the Zn deposition on the Pt substrate shown in Fig. 4b. The WAXS confirmed deposition of Zn on the Pt substrate. The strongest Zn peak for the (101) plane exhibited a measured d-spacing of 2.06 ± 0.01 Å and was near the expected value of 2.084 Å [46]. Note that the accuracy for d-spacing measurement was inferred from the measured d-spacing values for the Pt substrate and were within 0.01 Å of the expected values.

3.3. Zn deposition behavior within BMIm TfO

From the *in situ* AFM analysis, potentiostatic electrodeposition of Zn within the 0.34 mol kg^{-1} Zn(TfO)$_2$/BMIm TfO electrolyte resulted in zinc films with a dense and compact morphology composed of textured domains of stacked parallel hexagonal plates [30]. Because the geometry of the USAXS electrochemical cell differed from the AFM electrochemical cell, *ex situ* SEM images were obtained to check that the resulting Zn deposition morphology was consistent with that observed within the AFM cell. Fig. 5 shows representative SEM images of the zinc depositions where Fig. 5a was from the USAXS cell after 3600 Zn ML (1882.8 mC cm^{-2}) of charge passed, and Fig. 5b was from the AFM cell after 2800 Zn ML (1464 mC cm^{-2}) of charge passed. Both deposited surfaces exhibited compact domains consisting of stacked parallel hexagonal plates. Because the potentiostatic electrodeposition within the USAXS and AFM cell exhibited similar behavior, the domain size and plate thickness obtained from *in situ* AFM were quantitatively analyzed to help model the USAXS data.

3.3.1. Zinc domain size evolution

The domain size evolution was investigated by measuring the average domain sizes observed from both *in situ* AFM and *ex situ* SEM images. *In situ* AFM images were obtained from three
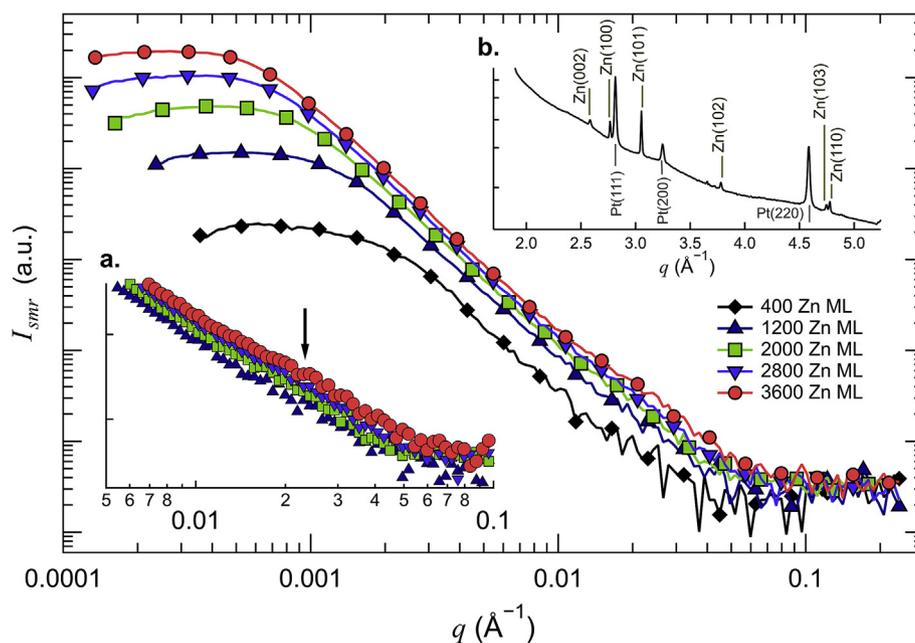
Fig. 4. Log-log plot of the slit smeared USAXS intensity versus the scattering vector, q, obtained from the USAXS scans after 400 Zn ML, 1200 Zn ML, 2000 Zn ML, and 3600 Zn ML of charge passed. Raw data have been background subtracted and the intensity is slit smeared with a slit-length of 0.027548 Å^1. An arrow in inset (a) highlights a small Guinier in the mid-q range. The scattering intensity measured from the WAXS image obtained after Zn deposition is shown in inset (b) including the corresponding diffraction planes for both Zn and Pt.
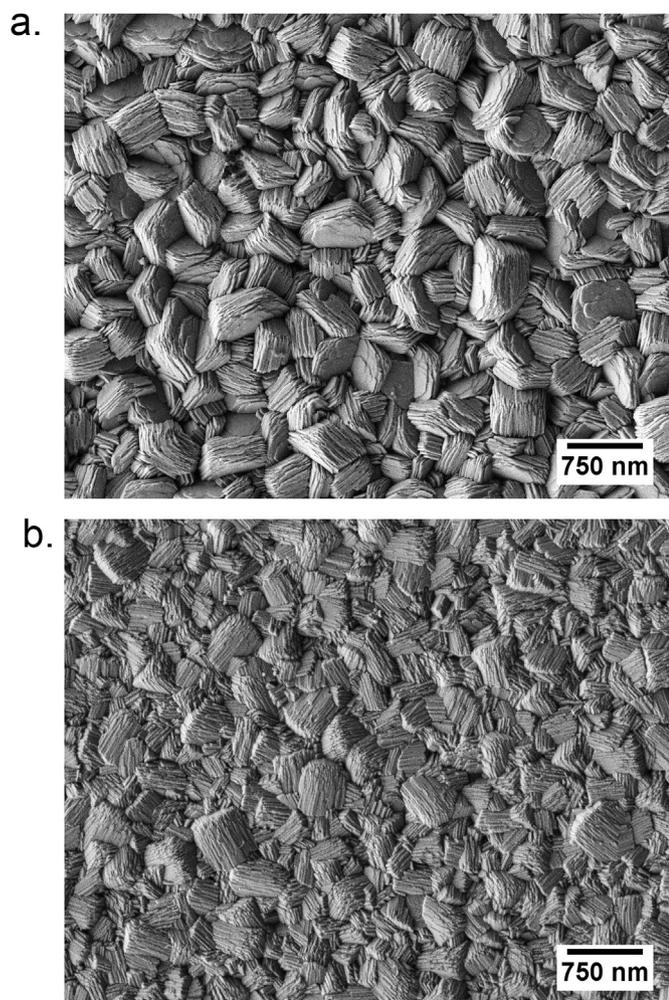
Fig. 5. SEM image of the zinc surface after deposition in 0.34 mol kg^{-1} Zn(TfO)$_2$/BMIm TfO (a) within the USAXS electrochemical cell with 3600 Zn ML (1882.8 mC cm^{-2}) of charge passed at a reducing potential of -370 mV vs. E_{CO}, and (b) within the AFM electrochemical cell with 2800 Zn ML (1464 mC cm^{-2}) of charge passed at a reducing potential of -325 mV vs. E_{CO}.

deposition trials with overpotentials of 244, 325, and 445 mV vs. E_{CO}, respectively. For each deposition trial, the average domain size was measured at images obtained from selected increments during deposition. For comparison, the average domain size was also measured from the *ex situ* SEM images of the zinc surface after deposition within the USAXS cell.

Representative AFM and SEM images that demonstrates the domain size growth of the zinc surface are shown in Fig. 6. AFM images obtained after 400, 1200, and 2800 Zn ML of charge passed is shown in Fig. 6a, b, and 6c, respectively. The average domain size was measured from the observed domains with examples outlined in Fig. 6e, f, and 6g. A representative SEM image obtained after deposition within the USAXS cell is shown in Fig. 6d with the corresponding domains observed outlined in Fig. 6h. Fig. 7a plots the average domain diameters measured from the AFM and SEM images as a function of nominal film thickness (amount of charge passed). At lower film thicknesses (400−1200 Zn ML) the diameter growth rate ranged from 0.07 to 0.10 nm ML^{-1} whereas for thicker films (2000−2800 Zn ML) the rate slowed, ranging from 0.01 to 0.09 nm ML^{-1}. Extrapolating the trends observed from the AFM measurements appeared to be consistent with the results obtained from the USAXS cell after 3600 Zn ML, further demonstrating that

the Zn deposition behavior within the USAXS cell was consistent with the behavior observed from the AFM cell.

We note that the average domain diameters measured from the 2D AFM and SEM images only approximate the true domain diameters due to two geometric effects. First the measured domain distribution was skewed towards smaller size as exemplified in Fig. 7b. The skewed distribution likely resulted from the fact that the widest part of individual Zn domains could be buried under neighboring Zn domains so that the image analysis would systematically underestimate the true domain size. This underestimate should be slightly offset, however, from the overestimate that occurs when measuring multiple domain orientations projected onto a 2D plane. To estimate the magnitude of this second effect, we approximated the domains as randomly oriented cylinders that were twice as wide as they were tall (R_c = cylinder radius = cylinder height). In this case, the domain measurements overestimated the true cylinder radii where $R_c \approx 0.9R$, where R is the measured domain radius from the 2D measurements.

3.3.2. Zinc plate nucleation and growth

During electrodeposition within the Zn(TfO)$_2$/BMIm TfO electrolyte, it was observed from the AFM images that new zinc islands preferentially nucleated on the basal facet of underlying hexagonal plates and these islands grew into new hexagonal plates. Subsequent nucleation on top of these new hexagonal plates resulted in zinc domains consisting of layers of co-aligned hexagonal plates. Fig. 8 shows a representative AFM image sequence obtained during electrodeposition highlighting several areas where new hexagonal zinc plates nucleated and grew on the basal facet of an underlying plate. Three examples of island nucleation can be seen in the upper half of Fig. 8b and in the lower left side of Fig. 8c. These nucleated plates continued to grow into new hexagonal plates as shown in Fig. 8c and d. As these new plates continued to grow, the basal facet of these new plates may reach a size large enough to allow for nucleation and growth of a new plate thus resulting in the overall growth into zinc domains of co-aligned plates as shown in the schematic in Fig. 8e. This type of nucleation and growth shown in Fig. 8e was also observed by Zheng et al. during electrodeposition of Zn where new Zn platelets exhibits a strong propensity to nucleate and grow on the exposed (0002) basal facet of the underlying Zn crystallite thereby highlighting the optimum atomic arrangement for epitaxial electrodeposition of Zn [47].

Although, in principle, nucleation of co-aligned islands describes homoepitaxial growth, we found that the islands did not grow monolayer by monolayer but rather as plates consisting of many atomic layers. In addition, the layered nature persisted and can be observed in the *ex situ* SEM images shown in Fig. 5 where the layers exhibited rough edges and striated domains. As discussed later in the USAXS analysis, we considered that some of the plates may have coalesced together during growth. If the plates merged or are homoepitaxial with no gap or change in density at the interface, the individual plates will not scatter X-rays.

The thin hexagonal plates appeared to exhibit roughly the same thickness during electrodeposition within the AFM cell regardless of the amount of charge passed or the amount of deposition overpotential. Plate thicknesses were measured from topographic AFM images of the zinc domains where the hexagonal basal facets of the zinc plates were oriented nearly parallel to the substrate. The example shown in Fig. 9 plots the height profiles along the top of the zinc plates within a domain after 1200 Zn ML of charge passed (Fig. 9a) and in the same domain after 2000 Zn ML of charge passed (Fig. 9b). Although zinc plates were continuously being added during deposition, the plate thickness measured from the height profiles maintained a relatively constant thickness of around 5 nm (~20 Zn ML).
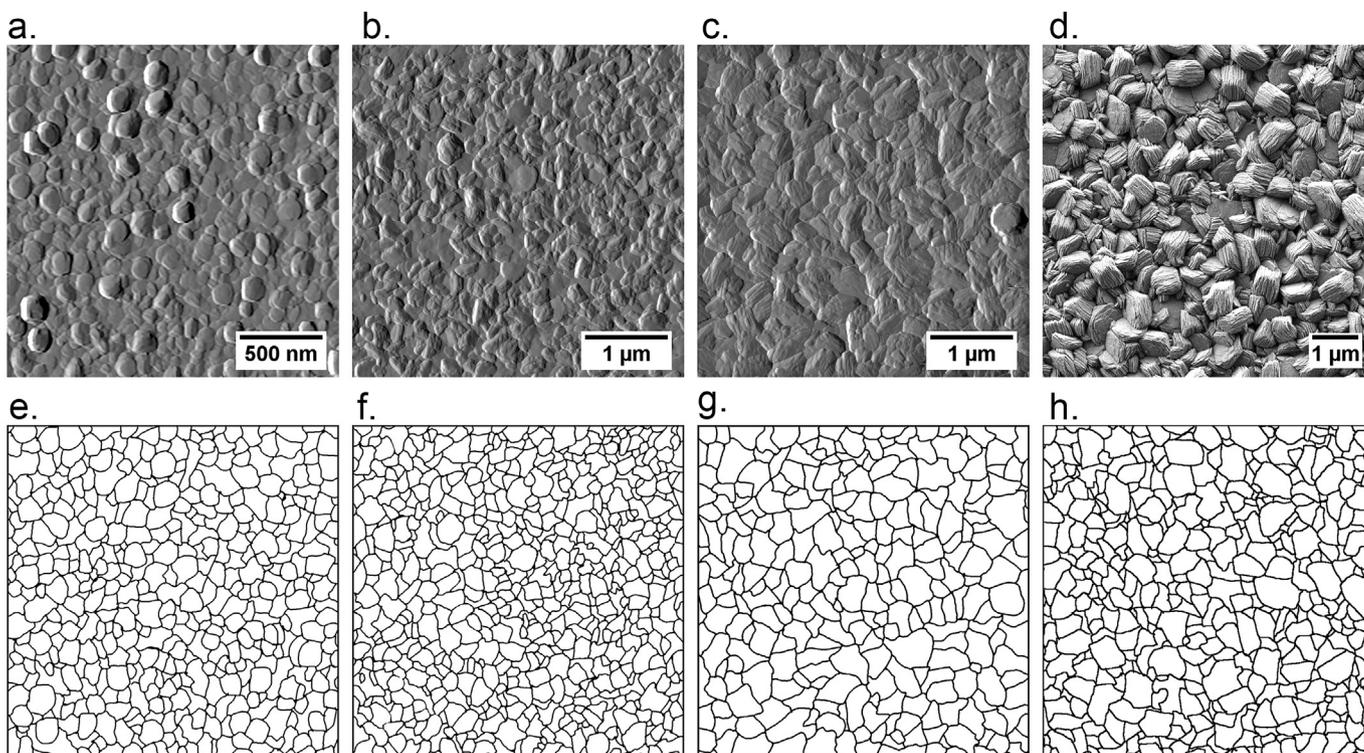
Fig. 6. Representative *in situ* AFM and *ex situ* SEM images where (a), (b), and (c) represents an AFM image (deflection) sequence of the zinc surface during electrodeposition within Zn(TfO)$_2$/BMIm TfO at a deposition overpotential of 445 mV vs. E_{CO} after 400 Zn ML (418.4 mC cm^{-2}), 1200 Zn ML (1255.2 mC cm^{-2}), and 2800 Zn ML (2928.8 mC cm^{-2}) of charge passed, and (d) is a representative SEM image from the Zn surface after electrodeposition within Zn(TfO)$_2$/BMIm TfO within the USAXS cell after 3600 Zn ML (1882.8 mC cm^{-2}) of charge passed. The observed domains are outlined for the corresponding AFM and SEM images in (e), (f), (g), and (h).

3.4. USAXS modeling

The *in situ* USAXS data (Fig. 4) contain information about the volume-average feature sizes of the deposit. Qualitatively, two separate Guinier knees were observed in the USAXS data. Only the low-q Guinier knee shifted in q, while the mid-q knee remained constant at $q \approx 0.02$ Å^{-1} with continued deposition. The relative intensity between each of these knees indicated that either the total volume or contrast of the low-q phase was always greater than the mid-q phase. From the AFM and SEM image analyses, we interpreted the Guinier regions observed in the X-ray scattering within low-q range as scattering from the zinc domains, and as these zinc domains grew with deposition thickness resulted in the Guinier shifting to lower q values. In addition, since the hexagonal zinc plates remained relatively constant in thickness during deposition with a thickness, t_p, of around 5 nm, we reasoned that the Guinier observed in the mid-q range is the result of X-ray scattering from these plate features.

Fig. 10 overviews the two paths followed in this investigation for modeling the USAXS data. The USAXS data is first described in terms of a generalized model (unified model) with scattering from the plate thickness and domain size. This can be visualized as isotropically-oriented cylinders with surface roughness due to plate edges. Since only a single-broadened Guinier region is observed at low-q, these cylinders are assumed to have moderate aspect ratios near unity and the radius of gyration of the domain represents the approximate dimensions of both diameter and height; two Guinier regions, separated by a power-law decay, would be observed for extreme large or small aspect ratios. The second approach modeled the USAXS data assuming the zinc deposition consisted of oriented cylinders (anisotropic model) composed of plates. The anisotropic model was an attempt to

capture the organization of plates into domains and the rotation of the domains from random orientations to more textured orientations that more closely mirrors the zinc morphology evolution observed from both the *in situ* AFM and *ex situ* SEM observations. The broad peak in intensity that precedes the low-q Guinier is attributed to the packing of the domains across the surface and is accounted for in both models by the simplest structure factor that is a function of the mean distance between domains and relative packing [45]. We note that other structure factors, such as one that assumes a Gaussian distribution in distances between domains [48], could also be used. The former structure factor was used for its simplicity.

3.4.1. Isotropic unified model

The USAXS data were fitted to a simple, isotropic model that accounted for two length scales representing both the plate thickness, t_p, and the plate radius, R_p. Data fits were used to extract the evolution of the zinc domain sizes, the individual plate thicknesses and the relative intensity scale between them. A two-level unified equation [33] with a constant background, b, was sufficient to approximate the scattering from the domains, $I_D(q)$, and the scattering from the plates, $I_p(q)$. The unified model describes scatter with a power law region and Guinier knee for each general feature size. When two length scales are present, as in the zinc electro-deposition data, two unified levels are merged consistently to generate a two-level unified fit as described in Equations (2)–(6):

$$I_{Zn}(q) = I_D(q) + I_p(q) + b \tag{2}$$

a.

b.
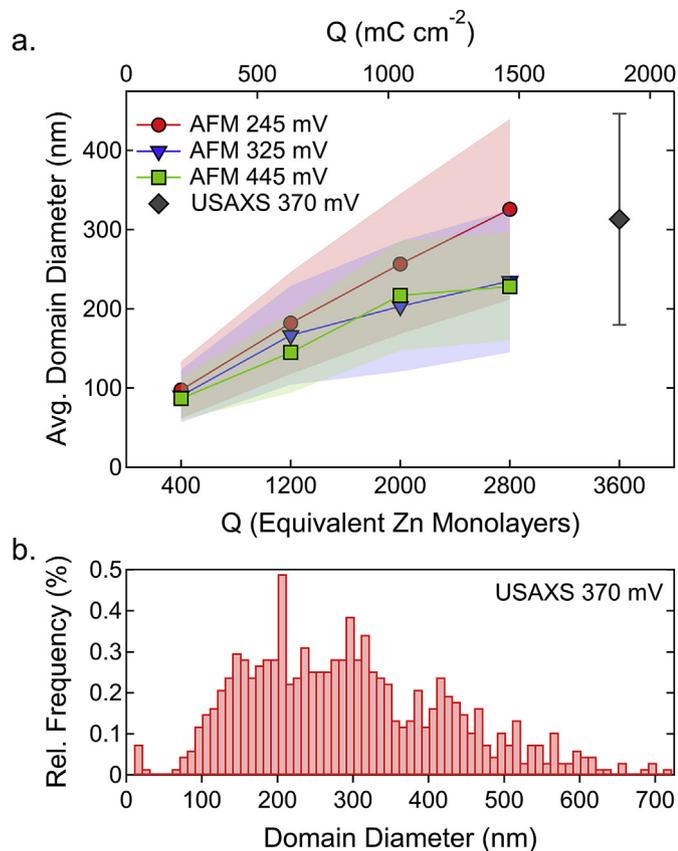
Fig. 7. (a) Average Zn domain diameters measured from *in situ* AFM imaging (AFM 245 mv, AFM 325 mV, and AFM 445 mv) and SEM images obtained from the Zn surface after deposition within the USAXS cell (USAXS 370 mV) plotted against the amount of charge passed. The shaded regions and horizontal bars represent the standard deviation range for the measured domain diameters. (b) Histogram showing the relative frequency of the domain diameters for the USAXS 370 mV data.
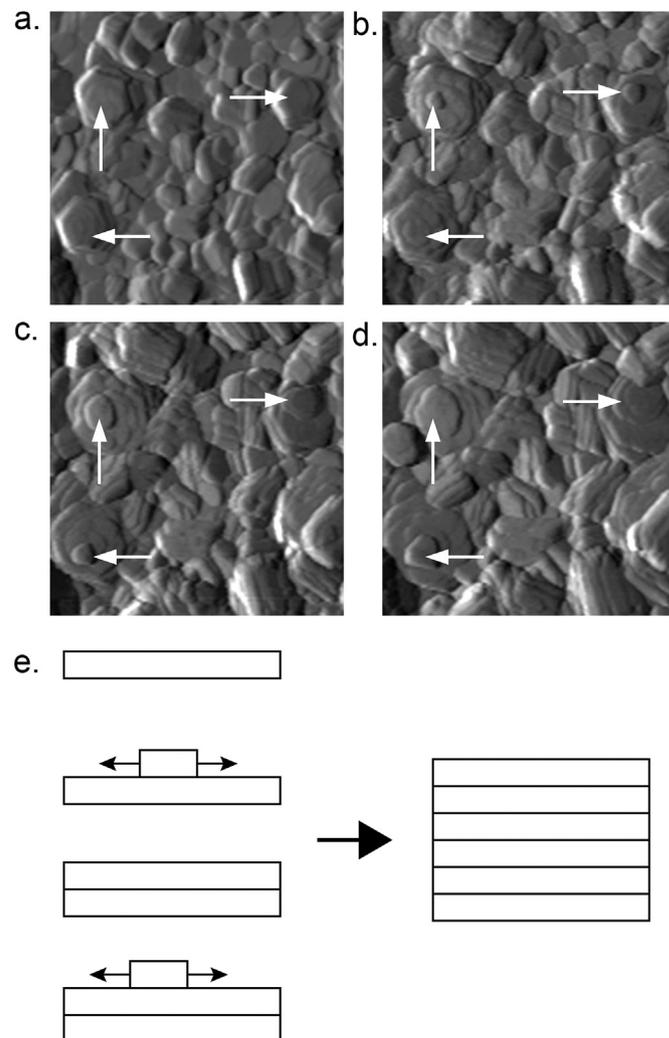

Fig. 8. AFM (deflection) image sequence of the zinc surface during electrodeposition within 0.34 mol kg^{-1} Zn(TfO)$_2$/BMIm TfO at a reducing potential of -325 mV vs. E_{CO} at amounts of charge passed of (a) 400 Zn ML (209.2 mC cm^{-2}), (b) 600 Zn ML (313.8 mC cm^{-2}), (c) 800 Zn ML (418.4 mC cm^{-2}), and (d) 1000 Zn ML (523.0 mC cm^{-2}). The AFM images are 1 μm × 1 μm. (e) Schematic showing how the preferential nucleation of islands on the basal facets could result in domains of co-aligned plates.

$$I_D(q) = S(q,p,\xi)\left[G_D e^{\frac{-q^2 R_{gD}^2}{3}} + B_D\left(\frac{\left(erf\left(\frac{qR_{gD}}{\sqrt{6}}\right)\right)^3}{q}\right)^{P_D}\right] \quad (3)$$

$$S(q,p,\xi) = \frac{1}{1+p\Phi(q\xi)} \quad (4)$$

$$I_p(q) = G_p e^{\frac{-q^2 R_{gp}^2}{3}} + B_p\left(\frac{\left(erf\left(\frac{qR_{gp}}{\sqrt{6}}\right)\right)^3}{q}\right)^4 \quad (5)$$

$$B_p = \frac{1.62 G_p}{R_g^{\ 4}} \quad (6)$$

where I_{Zn} represents the total scatter intensity, $S(q,p,\xi)$ is a structure factor that accounts for the apparent structure of the domains and uses the normalized scattering amplitude of a sphere, $\Phi(q\xi)$, and two parameters: p and ξ, that are related to the degree of crystallinity and mean distance between domains, respectively [45]; at low-q the apparent domain structure manifests itself in the "flatness" of the Guinier knee. The scaling parameters, G_D and G_p, are

the Guinier prefactors [33] proportional to the number, volume-squared and contrast-squared of the domains and plates, respectively; B_D and B_p are the prefactors for the power law behavior of the domains and plates, respectively; R_{gD} and R_{gp} are the radii of gyration for the domains and plates, respectively; and P_D is the power law exponent for the domains. We note that Equations (2), (3) and (5) assume that the two populations (domains and plates) scatter independently and therefore there is no "cutoff" term in Equation (3) that terminates the power-law scattering from the domains at high-q.

Equation (2) was fit to the slit-smeared intensity data using the Irena package [49] for Igor Pro to extract the parameters: R_{gD}, R_{gp}, G_D, G_p, B_D, P_D, b, p, and ξ. Our analysis used an isotropic structure factor and assumed that the domains were randomly oriented. This assumption was sufficient to extract the radii of gyration, using the Guinier approximation [45] within Equation (3) and Equation (5). The model fits for the USAXS data are shown in Fig. 11a.

In order to quantify the domain morphology, as measured by USAXS, the general parameters in Equation (2) were assigned to physical characteristics. For example, the radii of gyration, R_{gD} and
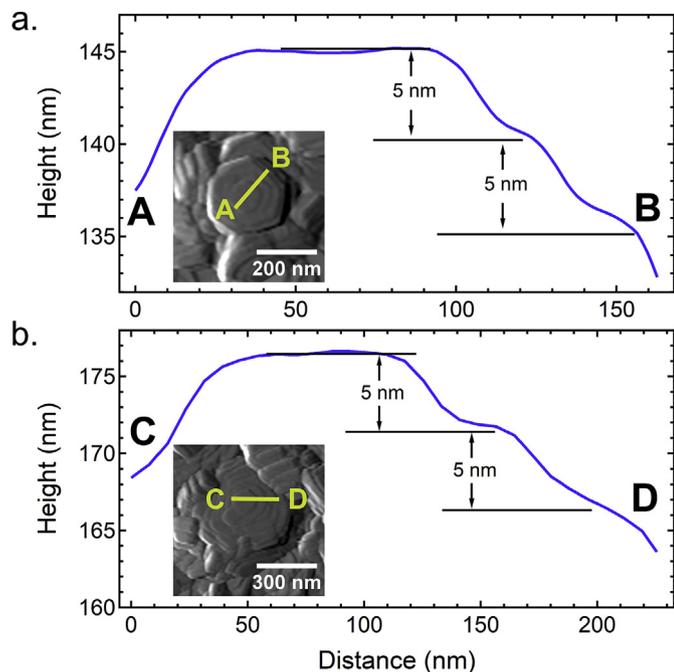
Fig. 9. Examples of AFM height profiles along zinc crystallite layers for the same zinc domain during deposition within 0.34 mol kg^{-1} Zn(TfO)$_2$/BMIm TfO at a reducing potential of -245 mV vs. E_{CO} growth after (a) 1200 Zn ML (627.6 mC cm^{-2}), and (b) 2000 Zn ML (1064.0 mC cm^{-2}) of charge passed. The letters designate the direction of the height profile.

R_{gp}, corresponds to the mean sizes of the domains and plates, respectively. The relative scales, G_D and G_p, also contain information about the scattering power of the plates within each domain. From the USAXS data, the low-q scattering from the zinc grain domains was much higher than the high-q scattering from the hexagonal plates. The minimal scattering in the high-q range for the plates suggested that the plates were coalesced together or the contrast between the plates was poorly defined. From the unified fit

parameters, the degree of coalescence, F^o, is defined as:

$$F^o = \frac{G_D}{V_D}\frac{V_p}{G_p} = \frac{\Delta\rho_D{}^2}{\nu_p\Delta\rho_p{}^2} \approx \frac{R_{gp}G_D}{R_{gD}G_p} \qquad (7)$$

$$\nu_p = \frac{N_pV_p}{N_DV_D} \qquad (8)$$

where ν_p is the volume fraction of individual plates per domain, N is the total number, V is the volume, and $\Delta\rho$ is the contrast of each respective phase; the ratio of the respective volumes was approximated by assuming the domains and plates had the same diameters, but different heights. When F^o is high, there is either a relatively low contrast between the plates or low volume fraction, ν_p, which would be this case for either partially or completely merged plates. On the other hand, when F^o is low, there is either good contrast between the plates or there is a high volume fraction of plates within the zinc domains. Therefore, a plot of F^o provides a measure of how well the plates coalesced together as more zinc was electrodeposited. The radii of gyration, R_{gp}, R_{gD}, and F^o are shown in Fig. 12a, b, and 12c, respectively, to quantify the evolution of the domain morphology with the amount of charge passed. Based on these plots, it was concluded that as the zinc grain domains grew, there was an increase in the degree of coalescence between the zinc plates within the domains.

3.4.2. Anisotropic oriented domain model

Though Equation (2) does not account for scattering anisotropy, it was sufficient to capture the dominant morphology changes during electrodeposition. In order to evaluate the fidelity of these results, we also developed an anisotropic model of oriented cylindrical domains [45] that contain a fraction of both coalesced (or merged) plates and discrete (or non-merged) plates. This model considers both the instrument geometry, slit smearing, and the orientation of the deposit. In addition, this formulation has one less fit parameter than Equation (2) since it uses the plate thickness from AFM measurements providing a physical link to the two
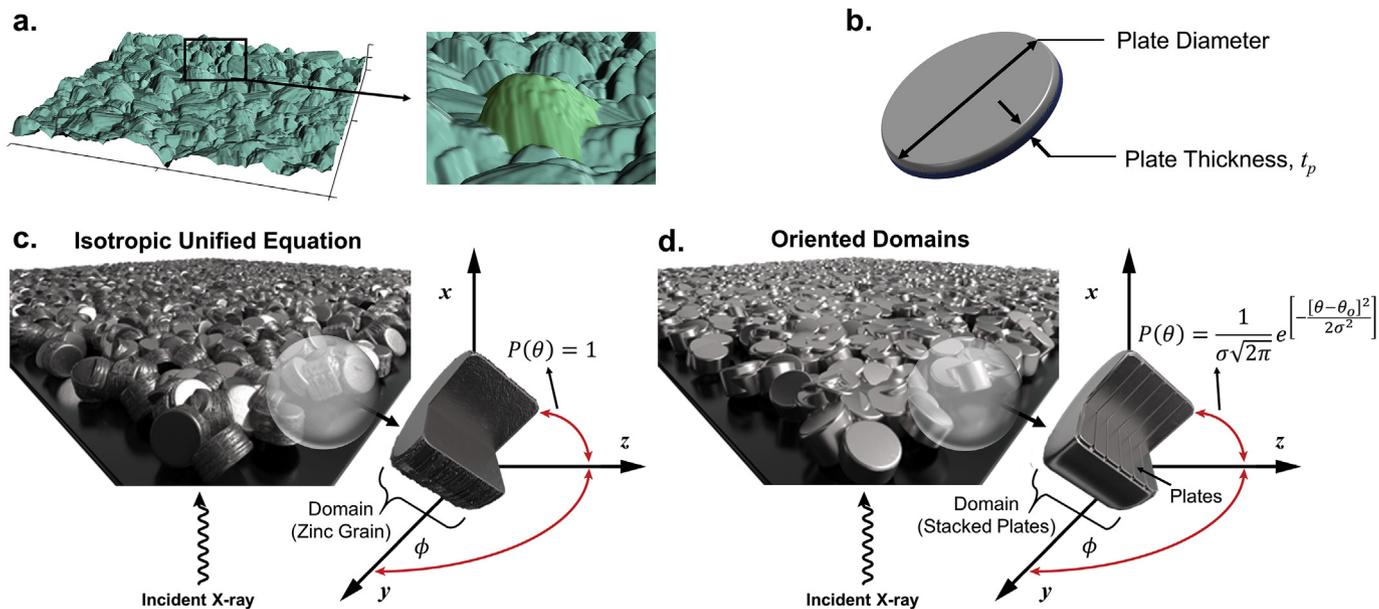
Fig. 10. (a) Representative AFM image of the zinc surface during electrodeposition within the 0.34 mol kg^{-1} Zn(TfO)$_2$/BMIm TfO electrolyte. (b) Simplified schematic of an individual zinc plate highlighting the plate diameter and plate thickness. Schematic showing the representative surface for the (c) isotropic unified model and the (d) anisotropic oriented domains model along with the scattering representation for individual zinc domains. In (c) and (d), the axes are defined such that the substrate is in the yz-plane and the X-rays propagate in the x direction.
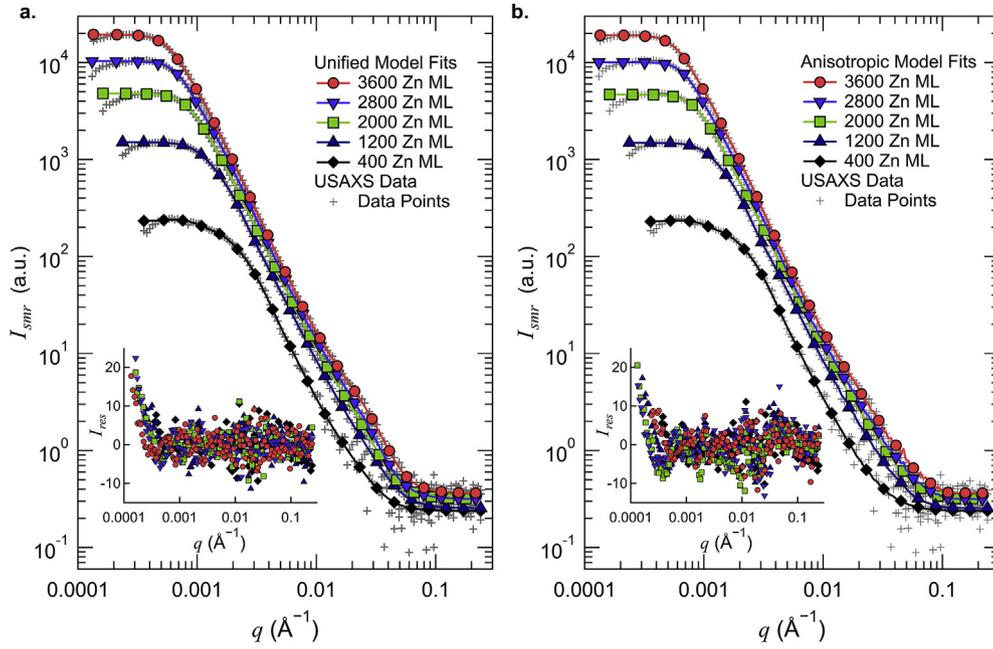
Fig. 11. The (a) unified model and (b) anisotropic model fits to the slit smeared USAXS intensity collected for the USAXS scans made after 400, 1200, 2000, 2800, and 3600 Zn ML of charge passed. The normalized residuals for the model fits is shown in the inset graphs within (a) and (b).

Guinier knees. A detailed explanation of this model can be found in the Supplemental. Briefly, the slit-smeared intensity data, $I_{smr}(q_z)$, was calculated by integrating the anisotropic scattering from oriented domains and plates, $I_{ODP}(\mathbf{q_R})$, over the slit-length that is defined by the instrument geometry [37]. With the Bonse-Hart instrument used in this study, the scattered intensity, $I(q_z)$, in the z direction was smeared with the scattered intensity in the y direction, $I(q_y)$, resulting in a smeared intensity that depended on the scatter vector with, $\mathbf{q_R}$ with a magnitude equal to $(q_z^2+q_y^2)^{1/2}$ [37]. The anisotropic scattering, $I_{model}(\mathbf{q_R})$, was calculated by assuming a Gaussian size distribution, $P_v(R, \overline{R}, \sigma)$, of cylindrical domains with a mean radius, $\overline{R}$, and standard deviation, σ; the height of the domains was parameterized by using an aspect ratio, A_r, such that the height is equal to $2RA_r$. Finally, the anisotropic scattering, $I_{ODP}(\mathbf{q_R})$, for a given radius, R, and q-vector, $\mathbf{q_R}$, was calculated by assuming a Gaussian distribution of orientations in the ϕ and θ directions, P_ϕ and P_θ,respectively [45]. The scattering model is given by the equations:

$$I_{smr}(q_z) = K \int_0^{q_{slit}} I_{model}\left(\mathbf{q_R}\left(q_y, q_z\right)\right)dq_y \qquad (9)$$

$$I_{model}\left(\mathbf{q_R}\left(q_y, q_z\right)\right) = S(q,p,\xi) \int_0^{\pi} \int_0^{\pi/2} P_\theta(\theta, \theta_0, \sigma_\theta)P_\phi(\phi, \phi_0, \sigma_\phi)$$
$$I_{ODP}\left(\mathbf{q_R}\left(q_y, q_z\right)\right)\sin\theta d\theta d\phi + b$$
$$\qquad (10)$$

$$I_{ODP}\left(\mathbf{q_R}\left(q_y, q_z\right)\right) = \sum_{R=0.1\overline{R}}^{R=10\overline{R}} V_{cyl}(R, RA_r)[I_{OD}(|\mathbf{q_R}|, R, \alpha) + I_{OP}(\times |\mathbf{q_R}|, R, \alpha)]P_v(R, \overline{R}, \sigma) \, \varDelta R$$
$$\qquad (11)$$

where V_{cyl} is the cylinder volume, and $S(q,\xi,p)$ is the same structure

factor as in Equation (4) that accounts for the apparent flatness in the low-q Guinier knee by assuming a distribution of preferred distances [50] between domains. To reduce the number of meaningful fit parameters and to facilitate a comparison of the results to Equation (2), the same values of b, p and ξ obtained from the fit of Equation (2) to each USAXS data were also used in Equation (10). The scattering from an oriented domain of plates, $I_{ODP}(\mathbf{q_R})$, was calculated by summing the volume-normalized scattering intensities from discrete, non-coalesced plates, $I_{OP}(\mathbf{q_R})$, and the entire domain, $I_{OD}(\mathbf{q_R})$, that consists of both coalesced and discrete plates. This summation allowed for the degree of coalescence, F^o, to be directly extracted from the model fitting (see Supplemental). The probability functions in Equation (10) were used to assign a weight to a specific orientation of the domains and plates determined by the angles ϕ and θ (Fig. 10), that together determine the angle, α, between the cylinder axis and $\mathbf{q_R}$. Based on the AFM images (Fig. 6), some preferential orientation in the angle, θ, is expected and therefore a Gaussian function was used for $P_\theta(\theta, \theta_0, \sigma_\theta)$, while $P_\phi(\phi, \phi_0, \sigma_\phi)$ was set to one for all angles. A value of $\sigma_\theta = 20°$ was used in the model fitting so that θ_o could be varied from its initial value of $45°$. Equation (10) can be used to find the optimal parameters for K, $\overline{R}$, σ, θ_o, v_{merged} and A_r by least-square fitting and the model fits for the USAXS data are shown in Fig. 11b. As shown in the residual plots in Fig. 11a and b, the same fit quality was obtained from both the unified model (Equation (2)) and from the anisotropic oriented domain model (Equation (10)).

The purpose of the anisotropic model was to determine if orientational anisotropy could account for the power-law behavior between the two Guinier knees, the large value of R_{gp} compared with AFM measurements, and if such anisotropy affected the growth and degree of coalescence obtained from the unified equation. Rather than shape dependent radii of gyrations, the anisotropic model provides size distributions of the cylinder radii and their aspect ratio (Supplemental). After 3600 Zn ML of charge passed, the mean cylinder diameter was found to be 500 nm, with a standard deviation of 225 nm. The value of A_r remained in the range: $0.45 < A_r < 0.55$ and did not change significantly with monolayer addition outside the fitting error, suggesting a squat

a.

b.

c.
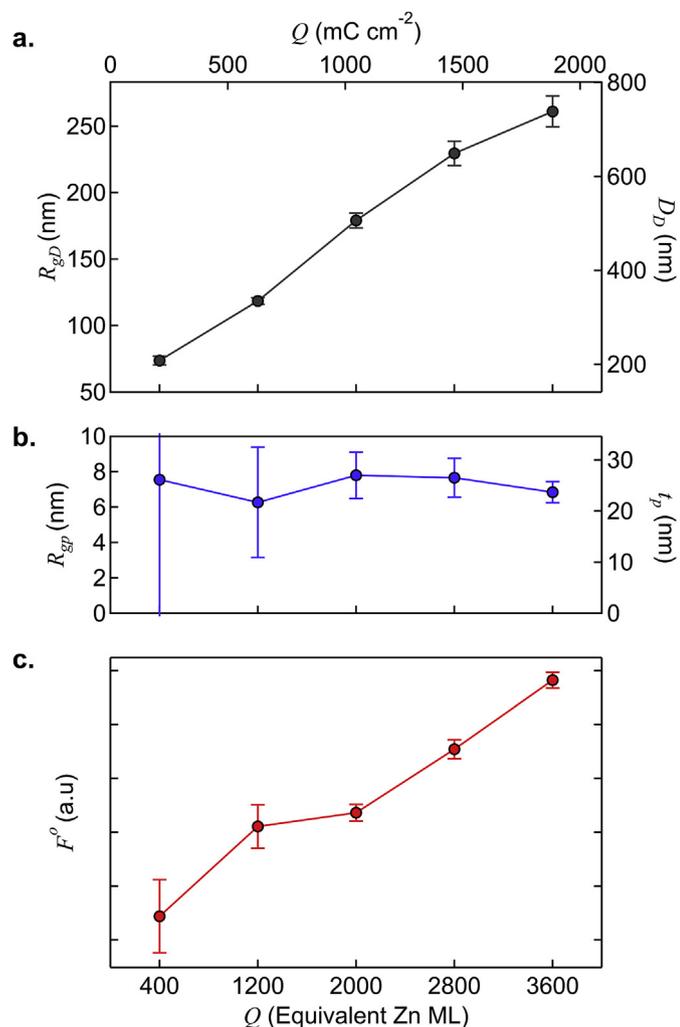
Fig. 12. Unified model fits of the radii of gyrations from the (a) domains and the (b) zinc plates, along with (c) the degree of plate coalescence, F^o, as a function of the zinc monolayers of charge passed. The horizontal bars represent the standard errors obtained from the least-squares linear fitting of the data within the Irena package for Igor pro.

cylinder twice as wide as tall. Therefore, both the domain diameter and height were consistent with measurements of the zinc domains from the AFM and SEM images (Fig. 7) and that the height of the domains as observed in the AFM experiments were less than the diameter [30]. From the SEM analysis of the domains after 3600 Zn ML of charge passed, the distribution of the domain diameters ranged from ~60 to 700 nm with a mean value of 313 ± 133 nm. The mean orientation angle, θ_o, decreases slightly from ~70° to 55° and was consistent with the SEM observations as shown in Fig. 5b where the Zn plates appeared to be closer to perpendicular to the surface after 2800 Zn ML of current passed. Therefore, the domain sizes and orientations obtained from the fitting of Equation (10) were in good agreement with the SEM and AFM observations.

From the unified model, the plate thickness, t_p, and the domain diameter, D_D, are related to the the radii of gyrations,

$$t_p = R_{gp}\sqrt{12} = 23 \ nm \tag{12}$$

$$D_D = 2R_{gD}\sqrt{2} = 735 \ nm \tag{13}$$

These mean values are larger than observed by AFM and SEM (Figs. 7 and 9). Therefore, the anisotropic model provides slightly better values for the domain dimensions and was able to accommodate a plate thickness closer to that which was measured by AFM imaging (Fig. 9). Other unified fit parameters, such as P_D and B_D, were difficult to quantitatively compare with parameters in the anisotropic model. However, it is worth noting that P_D never reached 4 with Equation (2) as expected for an anisotropic system [51], and the relative values of B_D and G_D suggested some size distribution [52]. Nevertheless, both the simple unified model (Equation (2)) and a more rigorous anisotropic model led to the same conclusion: as the zinc grains grow, the hexagonal plate thickness remained constant and more of the plates have coalesced together, since F^o increases with each Zn ML addition with either model (refer to Supplemental Fig. S3).

4. Conclusions

Electrodeposition of zinc in $Zn(TfO)_2$/BMIm TfO ionic liquid electrolyte resulted in a zinc morphology of a textured, hierarchically organized film consisting of co-aligned hexagonal plates organized into domains. AFM and SEM imaging along with X-ray scattering provided complementary views of the film evolution that give insight into the morphological progression and growth mechanism. In particular, the imaging and X-ray data suggested that this unusual film morphology develops due to 1) preferential nucleation of islands on the basal facets, that leads to domains; 2) anisotropic facet growth rates, that leads to texture; and 3) the coalescence of plates over time, that leads to dense granular films.

AFM imaging showed that the film progressed by island nucleation and growth of hexagonal plates that reflect the hexagonal symmetry of zinc. Two principle length scales emerged: the plate thickness and the plate diameter (which also becomes the domain diameter as the film thickens); these were measured by both AFM and X-ray techniques and compared. USAXS analysis showed similar trends to those observed by AFM. USAXS modeling by either the unified fit or the anisotropic model pointed to growth of the zinc grains, consistent with AFM observations. USAXS also showed that the thickness of the hexagonal zinc plates remained approximately constant during electrodeposition and confirmed observations made from AFM imaging. In addition, the USAXS data suggested that the zinc plates coalesced together over time thereby reducing scatter from the interior of the domains. This plate coalescence could not be directly observed from either AFM or SEM analysis.

Overall, a more complete picture emerged by using both direct imaging and X-ray techniques together: X-ray scattering provided better statistically averaged data and AFM imaging provided morphological details required to interpret the unified fit and to create more rigorous anisotropic models.

Declaration of competing interest

The authors declare that they have no known competing financial interests or personal relationships that could have appeared to influence the work reported in this paper.

CRediT authorship contribution statement

Jayme S. Keist: Conceptualization, Methodology, Investigation, Formal analysis, Writing - original draft. **Joshua A. Hammons:** Software, Formal analysis, Writing - review & editing. **Paul K. Wright:** Supervision. **James W. Evans:** Supervision, Writing - review & editing. **Christine A. Orme:** Conceptualization, Methodology, Investigation, Writing - review & editing, Supervision.

Acknowledgements

Appendix A. Supplementary data

Supplementary data to this article can be found online at https://doi.org/10.1016/j.electacta.2020.136073.

References

[1] F.R. McLarnon, E.J. Cairns, The secondary alkaline zinc electrode, J. Electrochem. Soc. 138 (2) (1991) 645−664.

[2] F. Beck, P. Ruetschi, Rechargeable batteries with aqueous electrolytes, Electrochim. Acta 45 (2000) 2467−2482.

[3] A.R. Mainar, E. Iruin, L.C. Colmenares, A. Kvasha, I. de Meatza, M. Bengoechea, O. Leonet, I. Boyano, Z. Zhang, J.A. Blazquez, An overview of progress in electrolytes for secondary zinc-air batteries and other storage systems based on zinc, Journal of Energy Storage 15 (2018) 304−328.

[4] M. Xu, D.G. Ivey, Z. Xie, W. Qu, Rechargeable Zn-air batteries: progress in electrolyte development and cell configuration advancement, J. Power Sources 283 (2015) 358−371.

[5] Y.G. Li, M. Gong, Y.Y. Liang, J. Feng, J.E. Kim, H.L. Wang, G.S. Hong, B. Zhang, H.J. Dai, Advanced zinc-air batteries based on high-performance hybrid electrocatalysts, Nat. Commun. 4 (2013).

[6] J.-S. Lee, S. Tai Kim, R. Cao, N.-S. Choi, M. Liu, K.T. Lee, J. Cho, Metal−air batteries with high energy density: Li−air versus Zn−air, Advanced Energy Materials 1 (1) (2011) 34−50.

[7] Y. Ito, M. Nyce, R. Plivelich, M. Klein, D. Steingart, S. Banerjee, Zinc morphology in zinc-nickel flow assisted batteries and impact on performance, J. Power Sources 196 (4) (2011) 2340−2345.

[8] L.F. Arenas, A. Loh, D.P. Trudgeon, X. Li, C. Ponce de León, F.C. Walsh, The characteristics and performance of hybrid redox flow batteries with zinc negative electrodes for energy storage, Renew. Sustain. Energy Rev. 90 (2018) 992−1016.

[9] R.V. Moshtev, P. Zlatilova, Kinetics of growth of zinc dendrite precursors in zincate solutions, J. Appl. Electrochem. 8 (1978) 213−222.

[10] Y. Oren, U. Landau, Growth of zinc dendrites in acidic zinc chloride solutions, Electrochim. Acta 27 (6) (1982) 739−748.

[11] W. Simka, D. Puszczyk, G. Nawrat, Electrodeposition of metals from non-aqueous solutions, Electrochim. Acta 54 (23) (2009) 5307−5319.

[12] M. Armand, F. Endres, D.R. MacFarlane, H. Ohno, B. Scrosati, Ionic-liquid materials for the electrochemical challenges of the future, Nat. Mater. 8 (8) (2009) 621−629.

[13] E.W. Castner, J.F. Wishart, Spotlight on ionic liquids, J. Chem. Phys. 132 (12) (2010).

[14] A.P. Abbott, G. Frisch, K.S. Ryder, Electroplating using ionic liquids, Annu. Rev. Mater. Res. 43 (2013) 335−358.

[15] F. Endres, F. Endres, D. MacFarlane, A. Abbott, Electrodeposition from Ionic Liquids, Wiley, 2008.

[16] D. Borissov, A. Pareek, F.U. Renner, M. Rohwerder, Electrodeposition of Zn and Au-Zn alloys at low temperature in an ionic liquid, Phys. Chem. Chem. Phys. 12 (9) (2010) 2059−2062.

[17] Q.B. Zhang, Y.X. Hua, Influence of [BMIM]HSO4 on electrodeposition and corrosion behavior of Zn coatings from acidic sulfate bath, Surf. Interface Anal. 44 (9) (2012) 1254−1260.

[18] J. Dogel, W. Freyland, Layer-by-layer growth of zinc during electrodeposition on Au(111) from a room temperature molten salt, Phys. Chem. Chem. Phys. 5 (12) (2003) 2484−2487.

[19] Z. Liu, S.Z. El Abedin, F. Endres, Electrodeposition of zinc films from ionic liquids and ionic liquid/water mixtures, Electrochim. Acta 89 (2013) 635−643.

[20] M. Xu, D.G. Ivey, W. Qu, Z. Xie, E. Dy, X.Z. Yuan, Zn/Zn(II) redox kinetics and Zn deposit morphology in water added ionic liquids with bis(trifluoromethanesulfonyl)imide anions, J. Electrochem. Soc. 161 (1) (2013) A128−A136.

[21] T.J. Simons, A.A.J. Torriero, P.C. Howlett, D.R. MacFarlane, M. Forsyth, High current density, efficient cycling of Zn2+ in 1-ethyl-3-methylimidazolium dicyanamide ionic liquid: the effect of Zn2+ salt and water concentration, Electrochem. Commun. 18 (C) (2012) 119−122.

[22] M.J. Deng, P.C. Lin, J.K. Chang, J.M. Chen, K.T. Lu, Electrochemistry of Zn(II)/Zn on Mg alloy from the N-butyl-N-methylpyrrolidinium dicyanamide ionic liquid, Electrochim. Acta 56 (17) (2011) 6071−6077.

[23] C. Fournier, F. Favier, Zn, Ti and Si nanowires by electrodeposition in ionic liquid, Electrochem. Commun. 13 (11) (2011) 1252−1255.

[24] M. Xu, D.G. Ivey, Z. Xie, W. Qu, Electrochemical behavior of Zn/Zn(II) couples in aprotic ionic liquids based on pyrrolidinium and imidazolium cations and bis(trifluoromethanesulfonyl)imide and dicyanamide anions, Electrochim. Acta 89 (2013) 756−762.

[25] Z. Liu, T. Cui, G. Pulletikurthi, A. Lahiri, T. Carstens, M. Olschewski, F. Endres, Dendrite-free nanocrystalline zinc electrodeposition from an ionic liquid containing nickel triflate for rechargeable Zn-based batteries, Angew. Chem. Int. Ed. 55 (8) (2016) 2889−2893.

[26] N. Li, H. Huang, W. Zhou, Reversible Zn/Zn2+ redox in [bmim] BF4+ H2O mixed system, ECS Transactions 59 (1) (2014) 371−378.

[27] T.J. Simons, D.R. MacFarlane, M. Forsyth, P.C. Howlett, Zn electrochemistry in 1-ethyl-3-methylimidazolium and N-butyl-N-methylpyrrolidinium dicyanamides: promising new rechargeable Zn battery electrolytes, ChemElectroChem 1 (10) (2014) 1688−1697.

[28] Y.-S. Wang, H.-W. Yeh, Y.-H. Tang, C.-L. Kao, P.-Y. Chen, Voltammetric study and electrodeposition of zinc in hydrophobic room-temperature ionic liquid 1-butyl-1-methylpyrrolidinium bis ((trifluoromethyl) sulfonyl) imide ([BMP] [TFSI]): a comparison between chloride and TFSI salts of zinc, J. Electrochem. Soc. 164 (2) (2017) D39−D47.

[29] T.J. Simons, P.M. Bayley, Z. Zhang, P.C. Howlett, D.R. MacFarlane, L.A. Madsen, M. Forsyth, Influence of Zn 2+and water on the transport properties of a pyrrolidinium dicyanamide ionic liquid, J. Phys. Chem. B 118 (18) (2014) 4895−4905.

[30] J.S. Keist, C.A. Orme, P.K. Wright, J.W. Evans, An in situ AFM Study of the evolution of surface roughness for zinc electrodeposition within an imidazolium based ionic liquid electrolyte, Electrochim. Acta 152 (2015) 161−171.

[31] U. Bonse, M. Hart, Tailless X-ray single-crystal reflection curves obtained by multiple reflection - (Si Ge crystals - E/T), Appl. Phys. Lett. 7 (9) (1965) 238−&.

[32] J. Ilavsky, A.J. Allen, L.E. Levine, F. Zhang, P.R. Jemian, G.G. Long, High-energy ultra-small-angle X-ray scattering instrument at the advanced photon source, J. Appl. Crystallogr. 45 (2012) 1318−1320.

[33] G. Beaucage, Approximations leading to a unified exponential power-law approach to small-angle scattering, J. Appl. Crystallogr. 28 (6) (1995) 717−728.

[34] M. Gnahm, D.M. Kolb, The purification of an ionic liquid, J. Electroanal. Chem. 651 (2) (2011) 250−252.

[35] B. El-Dasher, J.C. Farmer, S. Torres, S.G. Torres, Electrochemical Test Cell for Enabling In-Situ X-Ray Diffraction and Scattering Studies of Scale Formation and Microstructural Changes in Materials with Flow through Solution, 2014. United States.

[36] A.J. Bard, L.R. Faulkner, Electrochemical Methods: Fundamentals and Applications, Wiley, 2000.

[37] J. Ilavsky, P.R. Jemian, A.J. Allen, F. Zhang, L.E. Levine, G.G. Long, Ultra-small-angle X-ray scattering at the advanced photon source, J. Appl. Crystallogr. 42 (2009) 469−479.

[38] J. Ilavsky, F. Zhang, A.J. Allen, L.E. Levine, P.R. Jemian, G.G. Long, Ultra-small-angle X-ray scattering instrument at the Advanced Photon Source: history, recent development, and current status, Metall. Mater. Trans. 44A (1) (2013) 68−76.

[39] D. Nečas, P. Klapetek, Gwyddion: an open-source software for SPM data analysis, centr, Eur. J. Phys. 10 (1) (2012) 181−188.

[40] A. International, Standard Test Methods for Determining Average Grain Size, ASTM International, West Conshohocken, PA, 2013.

[41] K. Aoki, J. Osteryoung, Diffusion-controlled current at the stationary finite disk electrode: Theory, J. Electroanal. Chem. Interfacial Electrochem. 122 (1981) 19−35, 0.

[42] M. Galinski, A. Lewandowski, I. Stepniak, Ionic liquids as electrolytes, Electrochim. Acta 51 (26) (2006) 5567−5580.

[43] B. Scharifker, G. Hills, Theoretical and experimental studies of multiple nucleation, Electrochim. Acta 28 (7) (1983) 879−889.

[44] H.D. Bale, P.W. Schmidt, Small-angle X-ray-scattering investigation of submicroscopic porosity with fractal properties, Phys. Rev. Lett. 53 (6) (1984) 596−599.

[45] A. Guinier, G. Fournet, Small-angle Scattering of X-Rays, Wiley, New York, 1955.

[46] J. Nuss, U. Wedig, A. Kirfel, M. Jansen, The structural anomaly of zinc: evolution of lattice constants and parameters of thermal motion in the temperature range of 40 to 500 K, Z. Anorg. Allg. Chem. 636 (2) (2010) 309−313.

[47] J. Zheng, Q. Zhao, T. Tang, J. Yin, C.D. Quilty, G.D. Renderos, X. Liu, Y. Deng, L. Wang, D.C. Bock, Reversible epitaxial electrodeposition of metals in battery anodes, Science 366 (6465) (2019) 645−648.

[48] E.W. Huang, P.K. Liaw, L. Porcar, Y. Liu, Y.L. Liu, J.J. Kai, W.R. Chen, Study of nanoprecipitates in a nickel-based superalloy using small-angle neutron scattering and transmission electron microscopy, Appl. Phys. Lett. 93 (16) (2008) 3.

[49] J. Ilavsky, P.R. Jemian, Irena: tool suite for modeling and analysis of small-angle scattering, J. Appl. Crystallogr. 42 (2009) 347–353.

[50] R. Hosemann, S.N. Bagchi, The interference theory of ideal paracrystals, Acta Crystallogr. 5 (5) (1952) 612–614.

[51] O. Glatter, O. Kratky, Small Angle X-Ray Scattering, Academic Press, New York, New York, U.S.A, 1982.

[52] G. Beaucage, H.K. Kammler, S.E. Pratsinis, Particle size distributions from small-angle scattering using global scattering functions, J. Appl. Crystallogr. 37 (2004) 523–535.